

ARTICLE OPEN



TR12 centers in diamond as a room temperature atomic scale vector magnetometer

Jonas Foglszinger¹✉, Andrej Denisenko¹, Thomas Kornher², Matthias Schreck³, Wolfgang Knolle⁴, Boris Yavkin⁵, Roman Kolesov¹ and Jörg Wrachtrup¹

The family of room temperature atomic scale magnetometers is currently limited to nitrogen-vacancy centers in diamond. However, nitrogen-vacancy centers are insensitive to strong off-axis magnetic fields. In this work, we show that the well-known TR12 radiative defect in diamond, exhibits strong optically detected magnetic resonance (ODMR) signal under optical saturation. We also demonstrate that the spin system responsible for the magnetic resonance is an excited triplet state that can be coherently controlled at room temperature on a single defect level. The high optically detected magnetic resonance contrast, which is maintained even for strong off-axis magnetic fields, suggests that TR12 centers can be used for vector magnetometry even at high field.

npj Quantum Information (2022)8:65 ; <https://doi.org/10.1038/s41534-022-00566-8>

INTRODUCTION

Extending the field of quantum metrology i.e., magnetometry, electrometry, and thermometry to the atomic scale requires robust sensors with high sensitivity and spatial resolution. Optically addressable spins in diamond are excellent candidates as they often come with outstanding stability and narrow transitions, facilitating high sensitivity and nanometer resolution¹. The nitrogen-vacancy (NV) center has already proven its applicability to quantum sensing of magnetic and electric fields as well as temperature at nanometer scale^{2–4}. Unfortunately, strong magnetic fields lead to a mixing of the NV sub-levels which prevents effective spin initialization (spin pumping) for field-orientations not aligned with the NV symmetry axis. As a result, transitions within the NV center can no longer be observed in optically detected magnetic resonance measurement, hindering the sensing of strong magnetic fields for arbitrary orientations⁵.

Here, we present an extensive optically detected magnetic resonance study on individual TR12 centers in diamond which show much larger acceptance angle in high magnetic field and can sense magnetic fields up to several tens or even hundreds of mT for arbitrary orientation allowing for full vector magnetometry under ambient conditions. Even though there are hundreds of color centers known in diamond⁶, most of them do not facilitate spin control. Including different spin-free host materials some are known to allow for coherent spin manipulation under ambient conditions, namely, NV^{7–9} and ST1¹⁰ centers in diamond and silicon-vacancy (SiV) centers in 4H silicon carbide^{11,12}. Many other defects such as silicon-vacancy (SiV)^{13,14}, germanium-vacancy (GeV)¹⁵ or tin-vacancy (SnV)¹⁶ centers in diamond require low temperature cooling. To the best of our knowledge, only two defects are known to show high optically detected magnetic resonance contrast under ambient conditions i.e., room temperature: The NV center and the rather unknown ST1 center both in diamond. Here the TR12 center perfectly blends in as it shares this property and, unlike ST1, can be artificially created by electron irradiation and neutron or ion implantation^{17,18}. This facilitates the

creation of atomic scale or bulk probes based on TR12 centers, further extending sensing applications already established for the NV center.

Basic studies regarding the creation of TR12 centers as well as their spectroscopic properties were already performed in bulk measurements during the late twentieth century^{19–21}. An existence as high density ensembles combined with a negative correlation involving nitrogen suggests TR12 to be an intrinsic defect. The participation of interstitial atoms is also supported by the appearance of a local phonon mode²¹. Here we extend this work by rigorous studies on the spectroscopic and symmetry properties of single TR12 centers. In these studies performed under the condition of optical saturation we reveal the defect's electronic level structure as well as twelve inequivalent orientations of the center along with coherent properties of its associated spin in a metastable triplet state at room temperature. By measuring the optically detected magnetic resonance contrast for various magnetic field orientations we show the wide field susceptibility of the center for different field strengths. We also show that TR12 defect exhibits a static Jahn–Teller distortion leading to switching between two spatial configurations manifesting themselves as slight changes in the orientation of the local defect symmetry. Finally, we demonstrate that TR12 centers can be used to sense magnetic fields of almost arbitrary magnitude and orientation even at the level of a single TR12 defect. Such sensing capabilities at ambient conditions and with nanoscale spatial resolution are inaccessible by other defects in diamond (including NV center) and, moreover, in other hosts.

RESULTS

ODMR of TR12 centers in zero field

TR12 defects were identified in a confocal scan (see Fig. 1a) by measuring their emission spectra (see Fig. 1b). Their single nature was confirmed by the fluorescence antibunching signal shown in Fig. 1c. The auto-correlation signal at low excitation power yields

¹3rd Institute of Physics, University of Stuttgart, 70569 Stuttgart, Germany. ²Lumiphase AG, Brinerstrasse 21, 8003 Zürich, Switzerland. ³Institute of Physics, University of Augsburg, D-86135 Augsburg, Germany. ⁴Leibniz Institute for Surface Engineering (IOM), Department Functional Surfaces, D-04318 Leipzig, Germany. ⁵Quantronics Group, SPEC, CEA, CNRS, Université Paris-Saclay, 91191 Gif-sur-Yvette CEDEX, France. ✉email: jonas.foglszinger@pi3.uni-stuttgart.de

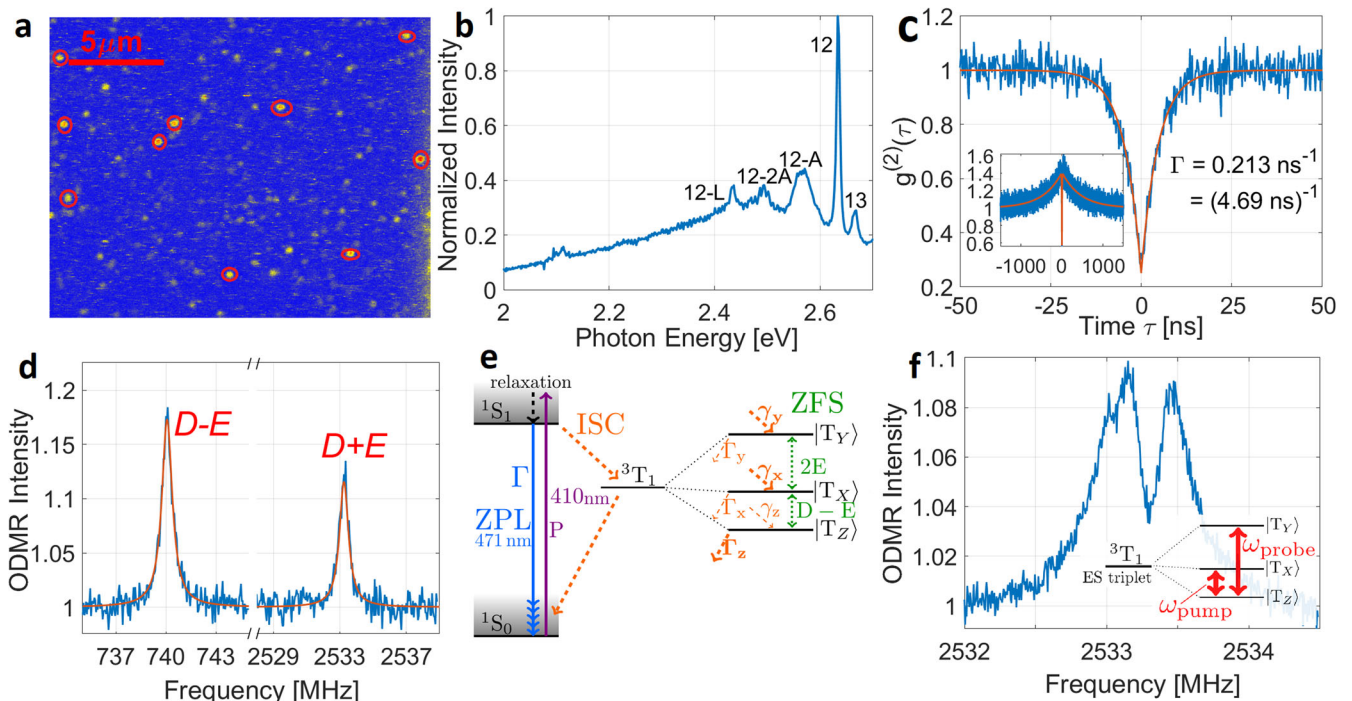


Fig. 1 Basic spectroscopic properties of TR12 centers. **a** Confocal scan image ($20\ \mu\text{m} \times 20\ \mu\text{m}$) of the sample. Most of the optically active defects visible in the image are TR12 defects, some of which are marked by red circles. **b** Fluorescence spectrum taken from a single TR12 center at room temperature, revealing a sharp zero phonon line (Label 12), a phonon side band in the hot tail (label 13), two replicas by acoustic phonons (labels 12-A, 12-2A) and a local phonon mode (label 12-L)²⁰. **c** Antibunching measurement well below saturation on a single TR12 center with dip at $\tau = 0$ below 0.5. The inset shows a corresponding long-lasting measurement at optical saturation revealing pronounced “bunching-shoulder” which does not appear at low excitation power. **d** Optically detected magnetic resonance spectrum in zero field. The contrast can reach up to 30% at high microwave power for both observed lines $D - E$ and $D + E$. **e** Proposed level structure for the TR12 defect with ground state and excited state singlet complemented by a metastable triplet in between. **f** Coherent population trapping resonance indicating the existence of two long-lived states T_x and T_y as pointed out in Supplementary Note 2.

an estimate of the emitting state lifetime of $4.7\ \text{ns}$ ²². Under the condition of optical saturation of the defect, the fluorescence intensity strongly increases (up to a factor of 2) upon application of a magnetic field. Together with long-lasting photon bunching at saturating optical excitation (see inset of Fig. 1c), this suggests the existence of a metastable optically populated electronic state^{10,22}. As a result, optically detected magnetic resonance should be observable for TR12 centers. Indeed, in zero magnetic field two sharp optically detected magnetic resonance lines can be observed at 740 and 2533.3 MHz as shown in Fig. 1d. The optically detected magnetic resonance contrast vanishes as the excitation laser power is reduced. To explain the observed optically detected magnetic resonance signal, at least three distinct spin states must be considered. The simplest non-trivial structure to fulfill this requirement involves ground and excited state singlets responsible for the emission and a metastable triplet state in between (see Fig. 1e). This natural guess supported from previous observations in molecules²³ and ST1¹⁰ turns out to be in perfect accordance with all further observations. The existence of exactly three distinct spin states in the metastable state was confirmed by investigating the dependence of the fluorescence intensity on the magnetic field (Supplementary Note 6). The spin Hamiltonian describing the triplet ($S = 1$) state in zero magnetic field is given by $H = D(S_z^2 - S(S + 1)/3) + E(S_x^2 - S_y^2)$, where $D = 1636.6\ \text{MHz}$ and $E = 896.6\ \text{MHz}$ can be deduced from the measured optically detected magnetic resonance resonance frequencies. It results in three spin states $|T_x\rangle$, $|T_y\rangle$, and $|T_z\rangle$ and, therefore, in three possible optically detected magnetic resonance transitions. In the experiment only two resonances were observed for different orientations for the center.

Investigating centers on various positions around the microwave antenna allowed to further manipulate the effective microwave polarization without observing more than two resonances. A wrong microwave polarization can therefore be excluded as possible cause and two of the three spin states must share the same lifetime. Since the positive optically detected magnetic resonance contrast is related to the redistribution of population from the long-lived occupied states to the short-lived empty states, there are two options: Either $|T_x\rangle$ and $|T_y\rangle$ are occupied and have longer lifetimes than $|T_z\rangle$ or vice versa. By applying constant microwave radiation at 740 MHz and sweeping a second microwave source through the second optically detected magnetic resonance resonance, we observe coherent population trapping (CPT) as shown in Fig. 1f. This indicates that there are two long-lived states, $|T_x\rangle$ and $|T_y\rangle$ as pointed out in Supplementary Note 2. From the width of the CPT resonance the lifetime of these long-lived states can be estimated to be 5 to $10\ \mu\text{s}$. The lifetimes of the triplet sub-levels can also be measured directly by observing the decay of the shelving-state population. For this the laser excitation was interrupted for a variable time τ allowing the metastable population to partially decay to the ground state singlet. This results in a temporal increase of the fluorescence once the laser excitation is restored. The dependence of this temporal increase on τ reveals the metastable lifetime. In Fig. 2a all states are monitored together, revealing only one exponential decay with a lifetime of $6.79\ \mu\text{s}$ fitting the estimation for the long-lived states $|T_x\rangle$ and $|T_y\rangle$. Consequently, the rate of intersystem crossing (ISC) into $|T_z\rangle$ is $\gamma_z \approx 0$, as $|T_z\rangle$ must be negligibly populated. To measure the lifetimes of $|T_x\rangle$ and $|T_y\rangle$ individually, one of them must be depleted by transferring its population to

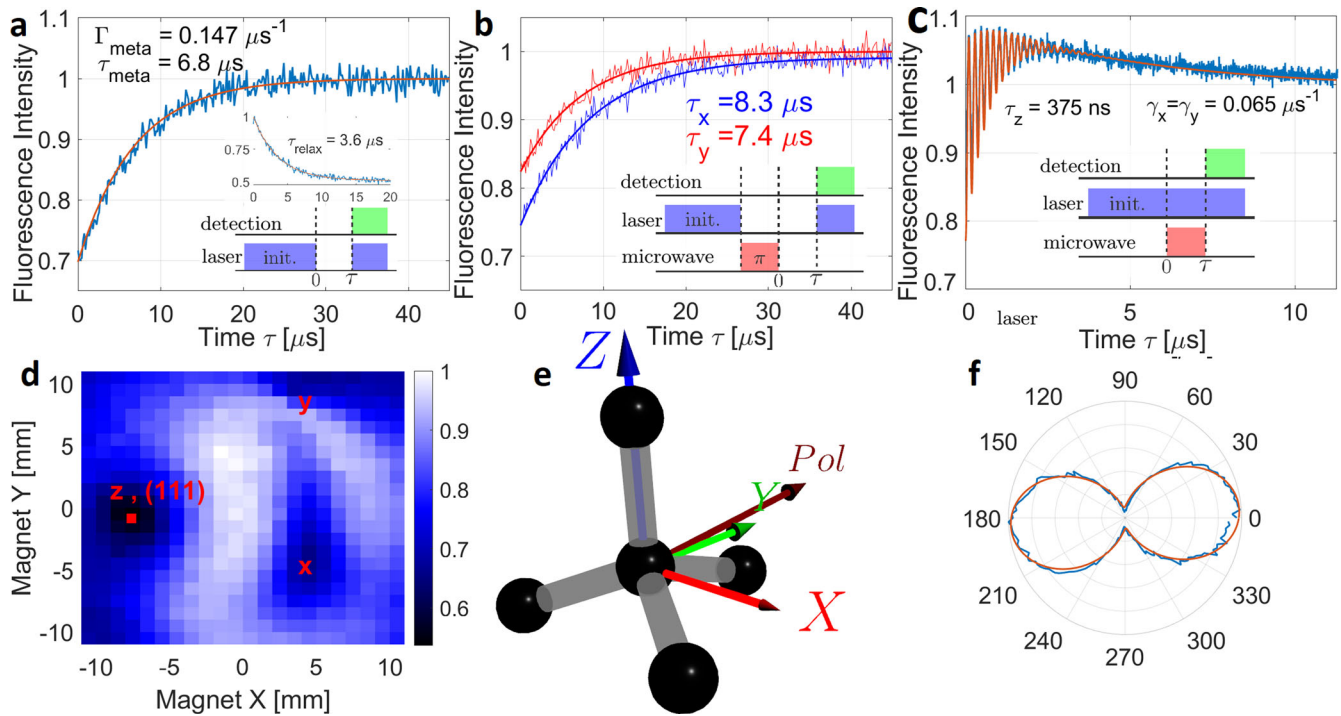


Fig. 2 Dynamics and orientations of singlet and triplet spin states. **a** Decay of the total metastable population. The inset shows the time-dependence of fluorescence intensity, when the metastable states are repopulated after initialization in the ground state. **b** Decay of metastable states T_x and T_y . **c** Rabi oscillation with full model fit pointed out in Supplementary Note 4. **d** Measured magnetic map for a TR12 center with marked [111] orientation in diamond and orientations for metastable triplet. **e** Illustration of TR12 triplet orientations and the fluorescing transition dipole vector in the diamond lattice. **f** Polarization-dependent fluorescence measurement for a single TR12 defect, revealing a single dipole transition.

the fast decaying state $|T_z\rangle$ with a microwave π -pulse (see Fig. 2b). In turn, the duration of a π -pulse is determined from microwave-induced Rabi oscillations (see Fig. 2c). The resulting lifetimes roughly fit the expected value from the overall decay. Figure 2b does only show a single exponential decay although the short-lived state $|T_z\rangle$ must have been populated. This is caused by an additional offset in time which was added deliberately to cut off the low resolution data from this decay. Instead τ_z was determined indirectly, by fitting it to the decay of the Rabi-oscillation between $|T_x\rangle$ and $|T_z\rangle$. To account for the overall dynamics of the system, a five level simulation (Supplementary Note 4) has been fitted to the data in Fig. 2c. By making the additional assumption about ISC rates into $|T_x\rangle$ and $|T_y\rangle$ $\gamma_x = \gamma_y$, not only the lifetime τ_z , but also these population rates can be extracted. This can be understood by considering the different timescales on which the respective effects take place. Rabi-oscillations decay within about 1 μ s, where $\tau_z = 375$ ns is fitted. On the other hand Fig. 2c shows that on a timescale of 5 to 10 μ s, a new steady fluorescence level is set. As this level is mostly defined by the rates into the metastable state $\gamma_x = \gamma_y = 0.065 \mu\text{s}^{-1}$, these values can be estimated. Simulations considering the overall optically detected magnetic resonance contrast, lead to the more precise values $\gamma_x = \gamma_y = 0.095 \mu\text{s}^{-1}$.

Fluorescence dependence on the magnetic field

Studying the dependence of the fluorescence on the external magnetic field provides further confirmation of the electronic level structure and gives insight into the symmetry of TR12 defects. For that, a permanent magnet ($10 \times 10 \times 10 \text{ mm}^3$ NdFeB, magnetization 1.4T perpendicular to the sample surface) is moved atop of the sample while the fluorescence intensity of the center is recorded depending on the magnet position. The dependence of the fluorescence on the magnetic field comes from mixing of the least

metastable $|T_z\rangle$ to $|T_x\rangle$ and/or $|T_y\rangle$ modifying their relaxation rates. This mixing is described by the Hamiltonian $H = D(S_z^2 - S(S+1)/3) + E(S_x^2 - S_y^2) + g\mu_B \mathbf{S} \cdot \mathbf{B}$ with zero-field splitting parameters D and E , the Bohr magneton μ_B , electron g-factor $g = 2$ and $S = 1^2$. An exemplary magnetic map is given in Fig. 2d. The dark spots on the map correspond to the orientations of the magnetic field not leading to mixing of $|T_z\rangle$ with at least one of the $|T_x\rangle$ and $|T_y\rangle$ states. The darkest spot marks the magnetic field pointing along the local z-axis of the center while the other two reveal the orientation of x- and y-axes. The results were compared to magnetic maps taken for NV centers in the same sample and revealed the z-axis being oriented close to [111] orientation in diamond (Supplementary Fig. 2a, b). Simulations of the magnetic maps showed that the y-axis of the TR12 is lying in the plane made by two adjacent σ -bonds. This fully defines the local frame of the center since the x-axis is perpendicular to z and y (see Fig. 2e). From the symmetries within the diamond lattice combined with simulations, we propose twelve inequivalent orientations for TR12 which were also confirmed in measurements. The corresponding magnetic maps are listed in Supplementary Fig. 3. Lastly, we studied the dependence of the fluorescence on the polarization of excitation light. The TR12 center has only one optical dipole as can be seen from the polarization-dependent fluorescence pattern shown in Fig. 2f. Even though only the projection of the dipole on the plane of the sample is measured directly, combining the projections for twelve magnetically inequivalent species allowed for unambiguous determination of the dipole direction in the local frame of the TR12 center. It appears to be slightly tilted with respect to the y-axis (see Fig. 2e).

Jahn–Teller effect

An evidence for strong coupling between electronic and vibrational degrees was presented in an earlier work by Davies²⁰.

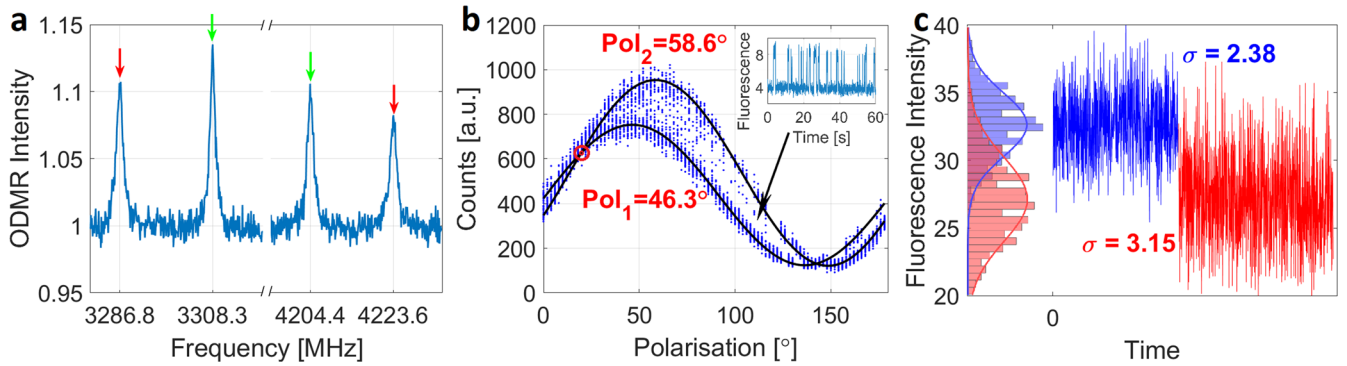


Fig. 3 Fluorescence dynamics resulting from Jahn-Teller distortion. **a** Anomalous splitting for both optically detected magnetic resonance resonances as a result of the center's local symmetry axes turning with respect to the magnetic field. Assigning the lines as indicated leads to the same magnetic field strength of 127.58 mT (± 0.01 mT). **b** Polarization-dependent fluorescence, supplemented by two fitted sine curves. The inset shows a lifetime trace from a single TR12 center for polarization of high contrast switching as indicated. The red circle marks the polarization angle of equal brightness at which the adjacent Fig. 3c was taken. **c** Fluorescence trace with two active microwave sources (blue) and one active microwave source (red). The overall noise increases although the shot-noise is reduced with the fluorescence amount. This increased noise is due to the switching between two different fluorescence levels which can not be resolved in time at high optical excitation power.

In the current work, we are providing further evidence to this complexity by demonstrating the following effects, which could eventually lead to identifying the structure of the TR12 center. First, we observe a splitting of the optically detected magnetic resonance lines of single TR12 into two under any external magnetic field which is identical for all centers sharing the same orientation. This cannot be explained by coupling to a nuclear spin since the number of split lines stays two at arbitrary orientation of the magnetic field. Indeed, nuclear spin-flip transitions should be allowed for arbitrarily oriented field and, therefore, for nuclear spin $I = 1/2$ one expects four resonances while we observe only two. At zero magnetic field no splitting could be observed. The second observation was made at low optical excitation, when telegraphic switching of the fluorescence intensity between two well defined levels was observed (see Fig. 3b inset). The dependence of the telegraphic signal on the polarization of laser excitation is shown in Fig. 3b. One can see two sinusoidal signals shifted by about 12° with the fluorescence intensity switching between them.

Both phenomena occurring jointly together can be explained if the TR12 center is hopping between two stable energetically degenerate configurations whose local symmetry axes are tilted with respect to each other. On the one hand, the optical dipole projection turns by about twelve degrees leading to different efficiency of laser excitation for a given polarization, which explains the telegraphic fluorescence signal. The switching becomes faster as the excitation power increases and is barely resolvable once the center is saturated. On the other hand, the splitting of the optically detected magnetic resonance line is caused by reorientation of the symmetry axes of the center with respect to the magnetic field. If both optically detected magnetic resonance lines are measured, one can always assign two pairs of resonances corresponding to exactly the same magnetic field strength (127.58 mT in Fig. 3a) meaning that the center is turning with respect to the B-field.

As the fluorescence switching can only be resolved at low excitation power, while optically detected magnetic resonance does only appear upon fluorescence saturation, there is no way to synchronize optically detected magnetic resonance and switching. A way to nevertheless link these two effects, is to set the polarization of the laser such that both dipoles make the same angle with the laser polarization. In this case, no switching is observable with none of the two split transitions or both driven by microwaves since both configurations are equally bright as indicated in Fig. 3b. However, if microwaves are applied in

resonance with only one of the two split transitions, switching is restored as only one of the configurations contributes to the optically detected magnetic resonance signal. Since switching is fast under optical saturation, this effect can be seen only as increased noise (see Fig. 3c).

The large singlet to singlet transition energy of TR12, more than half the band gap of diamond, makes ionization processes of the center very likely. The change between the two configurations could thus take place via intermediate ionization and subsequent recombination. It would also explain the dependence of the transition speed on the excitation intensity, since the center is more likely to be in the excited state for stronger excitation intensity and thus more likely to be ionized. This argument is also supported by Fig. 3b and inset, where the center proves to be more often in the state of lower fluorescence, i.e., lower excitation efficiency and thus lower ionization rate.

TR12 centers for quantum sensing of magnetic fields

One of the possible applications for TR12 centers is the measurement of magnetic fields with high sensitivity and high spatial resolution. Based on the proposed level structure in Fig. 1e the optically detected magnetic resonance contrast of TR12 centers can be calculated depending on magnetic field-strength and orientation (Supplementary Note 7). For a field-strength of 30 mT the results are illustrated in Fig. 4 and compared with the NV center. Since two resonance frequencies are required to determine the magnetic field strength in general², the figure displays the second highest contrast of all three optically detected magnetic resonance transitions. While NV centers are limited to sensing magnetic fields along their symmetry axis, TR12 can do so for almost arbitrary orientations with considerable contrast. Looking at bulk measurements, TR12 reveals further advantages. For full vector magnetometry with arbitrary orientations, optically detected magnetic resonance contrast of at least two different centers is required². As TR12 centers appear in twelve inequivalent orientations, even for strong magnetic fields, this condition can be fulfilled for almost arbitrary field-directions. While at 30 mT, bulk measurements would allow for full vector magnetometry for completely arbitrary orientations with at least 15% contrast (Supplementary Fig. 4), even at field strengths of 100 mT only small blind spots appear where the optically detected magnetic resonance contrast drops below 5% (see Fig. 5a). NV centers in contrast are limited to a rather small angular range (see Fig. 5b).

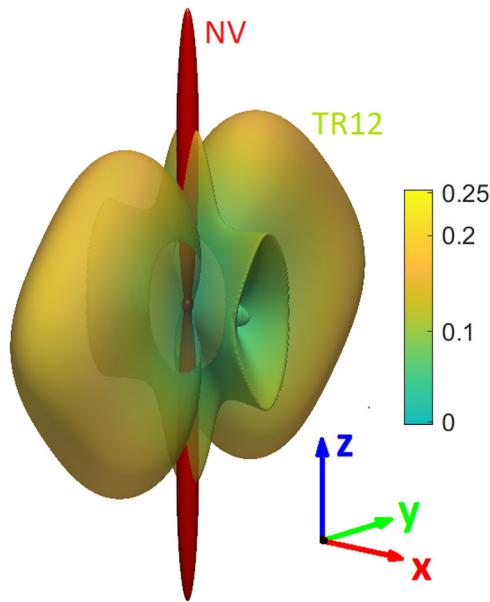


Fig. 4 ODMR contrast of a single TR12 center. Simulated optically detected magnetic resonance contrast as a function of the magnetic field orientation for TR12 (multicolored) and nitrogen-vacancy (red) for 30 mT. The figure displays the second highest optically detected magnetic resonance contrast of all three transitions available. The orientation of the TR12 metastable triplet is indicated by colored arrows.

This situation remains for field strengths of 1 T and beyond as displayed in Supplementary Fig. 4.

Given the setup used, magnetic field-strength and orientation are inseparably linked to each other in a rather complex way due to the permanent magnet. This prevents the isolation of one of these parameters and a consistency check for the simulations can only be performed for individual points. However, these measurements were carried out for various different magnetic fields and show excellent agreement. One of them is exemplarily shown in Fig. 5c and demonstrates the high optically detected magnetic resonance contrast for a strong field not aligned with any of the center's excited state axes for TR12 in contrast to NV (Fig. 5d).

We conclude, that indeed TR12 centers can be used for sensing magnetic field in a much wider angular range than NV centers even at high magnetic fields and would allow for direct full vector magnetometry in bulk measurements. The shot-noise limited magnetic sensitivity η for a single TR12 center can be estimated from the shot-noise $\sigma = 143$ counts per $\sqrt{\text{Hz}}$, the maximum gradient of the expected optically detected magnetic resonance spectrum $C_{\text{max}} = 1.3$ counts per kHz and the known frequency shift of optically detected magnetic resonance resonances of $C_M = 28$ GHz per T to be:

$$\eta = \frac{\sigma}{C_{\text{max}} C_M} = 3.9 \mu\text{T Hz}^{-1/2}, \quad (1)$$

for rather pessimistic 5% optically detected magnetic resonance contrast on top of 20 kcps fluorescence signal out of a single TR12 center and 1 MHz linewidth. The maximum gradient C_{max} is derived from the maximum derivative of an Lorentzian function with full width at half maximum of 1 MHz and amplitude of $10^4 \cdot 0.05$ counts.

DISCUSSION

The presence of a spin-active state of the TR12 defect in diamond has been demonstrated by means of confocal optically detected magnetic resonance spectroscopy. Detailed spectroscopic studies carried out on a large number of single defect centers allowed us

to collect enough statistics to propose an adequate model for the defect to describe its intriguing optical and spin properties. Twelve inequivalent orientations of the center in the diamond lattice are revealed by mapping its fluorescence as a function of external magnetic field. Additionally, we observed switching of the optical dipole of TR12 center between two distinct configurations and attributed this to static Jahn–Teller effect. This effect also shows as an anomalous splitting of optically detected magnetic resonance lines in external magnetic field.

The TR12 defect can be an interesting alternative to the NV center in diamond in quantum sensing and possibly quantum information processing. For sensing applications, TR12 center has its own pros and cons. It can be used to sense magnetic fields, temperature, strain, and, possibly, electric field, though its responsivity to temperature and electric field is still to be assessed. On one hand, since optically detected magnetic resonance is observed in the excited triplet state, the width of optically detected magnetic resonance resonances is intrinsically limited by its lifetime. Therefore, the sensitivity is limited fundamentally by the natural linewidth of the transition. On the other hand, TR12 has a much larger acceptance angle for measuring high magnetic fields on the order of tens of millitesla to Tesla. While NV centers can be used to sense the fields in this range only along its symmetry axis, the TR12 shows non-zero optically detected magnetic resonance contrast in a wide range of angles along all its excited triplet axes. Thus, TR12 can be used as a full vector nanoscale magnetometer for almost arbitrarily oriented B-field even in high field leading to possible applications such as precise calibration of magnetic resonance imaging scanners.

The defect also has some advantages over the NV center in quantum information processing. One can use it as a communication tool to initialize and read out nearby nuclear spin qubits (e.g., ^{13}C) once in the triplet state. However, the nuclear spin memories will not be affected by its spin when TR12 is in the ground state singlet. Thus, a longer nuclear memory lifetime is expected²⁴. Furthermore, strong zero phonon line (ZPL) of TR12 if enhanced by Purcell effect in a microcavity can serve as an interface between flying qubits (photons) and stationary ones (nuclear spins)²⁵. All this makes TR12 an interesting alternative and ally to the well-developed family of NV centers and IV-group divacancies for future studies and applications of solid-state optically active spin defects.

METHODS

Creation of TR12 centers

TR12 centers were created by either 10 or 370 keV ^{12}C ion implantation¹⁸ (10^{11} ions per cm^{-2}) or 10 MeV electron irradiation ($5 \cdot 10^{16}$ e^- per cm^{-2}) into (100) plane of chemical vapor deposition diamond followed by annealing at 800 °C for 1 h²⁶. While using ^{12}C ions allows for exact positioning, shallow implanted centers mostly lack the necessary photo-stability. Using higher implantation energies increases the average lifetime, but does not completely solve the problem. Centers created by electron irradiation have higher photo-stability but are randomly distributed over the sample. Beside the photo-stability, no spectroscopic difference was found between centers created by different methods. The presented data is therefore acquired from defects within both, ^{12}C ion implanted and electron irradiated samples.

Data acquisition

Defects were spectroscopically studied using a home-built confocal microscope with 410 nm linear polarized laser excitation schematically displayed in Supplementary Fig. 1. All experiments were performed at room temperature. The sample was scanned through the focal point by a 3D nano-positioner. The emitted fluorescence was split into two paths and detected by two single photon detectors for integral fluorescence and fluorescence auto-correlation measurements. Alternatively, the fluorescence could be deflected into a spectrometer for identification and spectral characterization of the emitters. Microwave radiation was supplied to the sample by a golden microwave waveguide lithographically defined

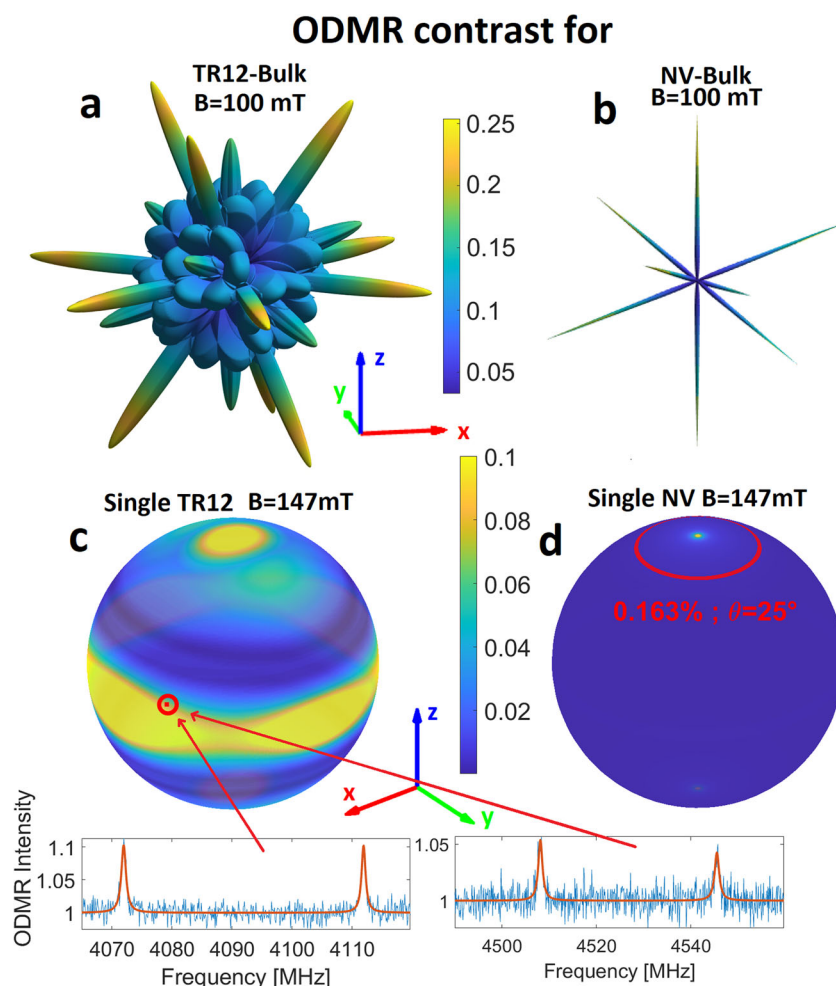


Fig. 5 TR12 centers in Bulk sample as vector magnetometer. **a** Optically detected magnetic resonance contrast of TR12 centers in Bulk considering the second highest optically detected magnetic resonance contrast of all TR12 orientations. More plots are given in the Supplementary Fig. 4. **b** Optically detected magnetic resonance contrast of nitrogen-vacancy centers considering the highest optically detected magnetic resonance contrast of all nitrogen-vacancy orientations. **c** Experimental confirmation of the adjacent simulation for orientations not aligned with any of the excited triplet axes at $B = 147$ mT. For the marked point, the simulated optically detected magnetic resonance contrast of 10.8% is divided between two lines resulting from the Jahn–Teller effect. Since the corresponding data in the insets were not corrected for background fluorescence, these measured intensities match the simulated value of 10.8%. **d** In comparison, the optically detected magnetic resonance intensity of the nitrogen-vacancy center would drop to almost 0.1% with the same misalignment of about 25% from its symmetry axis at $B = 147$ mT.

on the surface of the diamond. The setup was also equipped with a permanent magnet having magnetization perpendicular to the sample surface. Its position above the sample is controlled by high precision stepper motors. This allows the application of a magnetic field of variable magnitude and direction.

DATA AVAILABILITY

The data sets used to create the figures in the manuscript are available at <https://doi.org/10.5281/zenodo.6371917>. The remaining data sets supporting the findings of this study are available from the corresponding author upon reasonable request.

CODE AVAILABILITY

The MATLAB simulation code that supports the findings of this work is available from the corresponding author upon reasonable request.

Received: 15 September 2021; Accepted: 8 April 2022;

Published online: 02 June 2022

REFERENCES

1. Staudacher, T. et al. Nuclear magnetic resonance spectroscopy on a (5-nanometer)³ sample volume. *Science* **339**, 561–563 (2013).
2. Balasubramanian, G. et al. Nanoscale imaging magnetometry with diamond spins under ambient conditions. *Nature* **455**, 648–651 (2008).
3. Dolde, F. et al. Electric-field sensing using single diamond spins. *Nat. Phys.* **7**, 459–463 (2011).
4. Kucsko, G. et al. Nanometre-scale thermometry in a living cell. *Nature* **500**, 54–58 (2013).
5. Tetienne, J.-P. et al. Magnetic-field-dependent photodynamics of single nv defects in diamond: an application to qualitative all-optical magnetic imaging. *New J. Phys.* **14**, 103033 (2012).
6. Zaitsev, A. *Optical Properties of Diamond* 1st edn (Springer, 2001).
7. Acosta, V. M. et al. Dynamic stabilization of the optical resonances of single nitrogen-vacancy centers in diamond. *Phys. Rev. Lett.* **108**, 206401 (2012).
8. Fuchs, G. D. et al. Excited-state spin coherence of a single nitrogen–vacancy centre in diamond. *Nat. Phys.* **6**, 668–672 (2010).
9. Shen, Y., Sweeney, T. M. & Wang, H. Zero-phonon linewidth of single nitrogen vacancy centers in diamond nanocrystals. *Phys. Rev. B* **77**, 033201 (2008).
10. Lee, S.-Y. et al. Readout and control of a single nuclear spin with a metastable electron spin ancilla. *Nat. Nanotechnol.* **8**, 487–492 (2013).

11. Baranov, P. G. et al. Silicon vacancy in sic as a promising quantum system for single-defect and single-photon spectroscopy. *Phys. Rev. B* **83**, 125203 (2011).
12. Nagy, R. et al. High-fidelity spin and optical control of single silicon-vacancy centres in silicon carbide. *Nat. Commun.* **10**, 1954 (2019).
13. Neu, E. et al. Fluorescence and polarization spectroscopy of single silicon vacancy centers in heteroepitaxial nanodiamonds on iridium. *Phys. Rev. B* **84**, 205211 (2011).
14. Liu, A. & Cundiff, S. T. Spectroscopic signatures of electron-phonon coupling in silicon-vacancy centers in diamond. *Phys. Rev. Mater.* **4**, 055202 (2020).
15. Siyushev, P. et al. Optical and microwave control of germanium-vacancy center spins in diamond. *Phys. Rev. B* **96**, 081201(R) (2017).
16. Trusheim, M. E. et al. Transform-limited photons from a coherent tin-vacancy spin in diamond. *Phys. Rev. Lett.* **124**, 023602 (2020).
17. Clark, C. D., Ditchburn, R. & Dyer, H. The absorption spectra of natural and irradiated diamonds. *Proc. Math. Phys. Eng. Sci.* **234**, 363–381 (1956).
18. Naydenov, B. et al. Engineering single photon emitters by ion implantation in diamond. *Appl. Phys. Lett.* **95**, 181109 (2009).
19. Walker, J. An optical study of the TR12 and 3h defects in irradiated diamond. *J. Phys. C: Solid State Phys.* **10**, 3031–3037 (1977).
20. Davies, G., Foy, C. & O'Donnell, K. The TR12 vibronic band in diamond. *J. Phys. C: Solid State Phys.* **14**, 4153–4165 (1981).
21. Mainwood, A., Collins, A. T. & Woad, P. Isotope dependence of the frequency of localized vibrational modes in diamond, in *Defects in Semiconductors 17*, Materials Science Forum, Vol. 143, (eds Heinrich, H. & Jantsch, W.) 29–34 (Trans Tech Publications Ltd, 1993).
22. Berthel, M. et al. Photophysics of single nitrogen-vacancy centers in diamond nanocrystals. *Phys. Rev. B* **91**, 035308 (2015).
23. Wrachtrup, J., von Borczyskowski, C., Bernard, J., Orrit, M. & Brown, R. Optically detected spin coherence of single molecules. *Phys. Rev. Lett.* **71**, 3565–3568 (1993).
24. Wang, P. & Yang, W. Theory of nuclear spin dephasing and relaxation by optically illuminated nitrogen-vacancy center. *New J. Phys.* **17**, 113041 (2015).
25. Riedrich-Möller, J. et al. Nanoimplantation and Purcell enhancement of single NV centers in photonic crystal cavities in diamond. *Appl. Phys. Lett.* **106**, 221103 (2015).
26. Iakubovskii, K. & Adriaenssens, G. Optical study of some interstitial-related centres in cvd diamond. *Phys. Status Solidi (a)* **181**, 59–64 (2000).

ACKNOWLEDGEMENTS

We thank Adam Gali, Kangwei Xia and Denis Dertli for fruitful discussions and help with the preparation of the manuscript. This work was supported by Bundesministerium für Bildung und Forschung (project UNIQ), Deutsche Forschungsgemeinschaft (grant KO4999/3-1), FET-Flagship Project SQUARE, ERC grant SMel, EU project ASTERIQS, DFG research group FOR 2724 and QTBW.

AUTHOR CONTRIBUTIONS

The experiments were performed by J.F. with support from R.K. and J.W. Simulations were carried out by J.F. and R.K. The evaluation was done by J.F. with strong support from R.K. as well as J.W. and all other authors. A.D., T.K., M.S., and W.K. produced and processed diamond samples for the experiments and provided associated information. B.Y. helped building the setup in the initial phase of the experiments. The manuscript was written by J.F. and R.K. with input from all other authors.

FUNDING

Open Access funding enabled and organized by Projekt DEAL.

COMPETING INTERESTS

The authors declare no competing interests.

ADDITIONAL INFORMATION

Supplementary information The online version contains supplementary material available at <https://doi.org/10.1038/s41534-022-00566-8>.

Correspondence and requests for materials should be addressed to Jonas Foglszinger.

Reprints and permission information is available at <http://www.nature.com/reprints>

Publisher's note Springer Nature remains neutral with regard to jurisdictional claims in published maps and institutional affiliations.



Open Access This article is licensed under a Creative Commons Attribution 4.0 International License, which permits use, sharing, adaptation, distribution and reproduction in any medium or format, as long as you give appropriate credit to the original author(s) and the source, provide a link to the Creative Commons license, and indicate if changes were made. The images or other third party material in this article are included in the article's Creative Commons license, unless indicated otherwise in a credit line to the material. If material is not included in the article's Creative Commons license and your intended use is not permitted by statutory regulation or exceeds the permitted use, you will need to obtain permission directly from the copyright holder. To view a copy of this license, visit <http://creativecommons.org/licenses/by/4.0/>.

© The Author(s) 2022